

2014-01-01

3D Printing Technology Using High Viscous Materials-Synthesis Of Functional Materials And Fabrication Of 3D Metal Structure

Seongik Hong

University of Texas at El Paso, hong.sung.ik@gmail.com

Follow this and additional works at: https://digitalcommons.utep.edu/open_etd



Part of the [Materials Science and Engineering Commons](#), and the [Mechanics of Materials Commons](#)

Recommended Citation

Hong, Seongik, "3D Printing Technology Using High Viscous Materials-Synthesis Of Functional Materials And Fabrication Of 3D Metal Structure" (2014). *Open Access Theses & Dissertations*. 1258.
https://digitalcommons.utep.edu/open_etd/1258

This is brought to you for free and open access by DigitalCommons@UTEP. It has been accepted for inclusion in Open Access Theses & Dissertations by an authorized administrator of DigitalCommons@UTEP. For more information, please contact lweber@utep.edu.

3D PRINTING TECHNOLOGY USING HIGH VISCOUS MATERIALS
- SYNTHESIS OF FUNCTIONAL MATERIALS AND
FABRICATION OF 3D METAL STRUCTURE

SEONGIK HONG

Department of Metallurgical and Materials Engineering

APPROVED:

Namsoo Peter Kim, Ph.D., Chair

Roy Arrowood, Ph.D.

Raymond C. Rumpf, Ph.D.

Charles Ambler, Ph.D.

Dean of the Graduate School

Copyright ©

by

Seongik Hong

2014

3D PRINTING TECHNOLOGY USING HIGH VISCOUS MATERIALS
- SYNTHESIS OF FUNCTIONAL MATERIALS AND
FABRICATION OF 3D METAL STRUCTURE

by

SEONGIK HONG BS in MME

THESIS

Presented to the Faculty of the Graduate School of

The University of Texas at El Paso

in Partial Fulfillment

of the Requirements

for the Degree of

Master of Science

Department of Metallurgical and Materials Engineering

THE UNIVERSITY OF TEXAS AT EL PASO

December 2014

Acknowledgements

This work was supported by NSF-NUE: Printing Innovative Nano-Engineering Technology Research and Elite Education (PINE TREE) (grant number: 1343607).

Printing Nano Engineering Lab Team

Mr. Seyeon Hwang

Mr. Cesar Sanchez

Mr. Edgar Reyes

Ms. Paola G. Barraza

Mr. Hanuel Du

Ms. Haryung Choi

Dr. Namsoo Peter Kim

The University of Texas at El Paso

Abstract

In the 3D printing technology, the research for using various materials has been performing. In this research work, 3D printable high viscous materials are suggested as one of the solutions for problems in the traditional 3D printing technology.

First, Cu-Ag coreshell was synthesized as a functional material. In terms of the reaction rate, reaction rate limiting step was defined as a fundamental research, and then prepared Cu-Ag coreshell was printed and analyzed. Second, the high viscous Cu paste was prepared and then metal 3D printed structure was fabricated by using new printing method.

In the synthesis of Cu-Ag coreshell, different sizes of Cu particle, 2 μ m and 100nm were used, and when 2 μ m Cu was applied, the reaction rate was limited by film diffusion control. However, when 100nm Cu was applied, reaction rate was controlled by CuO film and the rate of the reaction, which includes removing CuO film in the solution, is limited by chemical reaction control. The shape of Cu-Ag particle is spherical in the 2 μ m Cu condition and dendrite shape in the 100nm Cu condition respectively. The conductivity of Cu-Ag coreshell paste increased as increasing content of coreshell particle in the paste and sintering temperature.

In order to print high viscous metal paste, the high viscous Cu paste was printed by using screw extruder, and the viscosity of Cu paste was measured as a fundamental research. As increasing wt.% of Cu in the paste, the viscosity also increased. In addition, the shrinkage factor was reduced by increasing wt.% of Cu in the paste. An optimized printing condition for the high viscous material was obtained, and by using this condition, 3D metal structure was fabricated. The final product was heat treated and polished. Through these processes, a fine quality of metal 3D structure was printed.

Table of contents

Acknowledgment	iv
Abstract	v
Table of contents	vi
List of table	vii
List of figures	viii
Chapter	
1 Introduction.....	1
1.1 Part 1: Synthesis of functional material: Cu-Ag coreshell	3
1.2 Part 2: High viscous material for 3D printing technology	4
2 Materials and experimental procedure	7
2.1 Part 1: Materials	7
2.2 Part 1: Experimental procedure	7
2.3 Part 2: Materials	18
2.4 Part 2: Experimental procedure	18
3 Results and discussion	21
3.1 The limiting step of reaction	21
3.2 The Shape and cementation ratio of Cu-Ag coreshell.....	39
3.3 Electrical conductivity measurement	41
3.4 Viscosity of high viscous Cu paste	49
3.5 Printing process and optimization of parameters for 3D metal structure.....	55
3.6 Packing factor effect on fabrication of 3D metal structure	61
4 Conclusion	64
References	67
Curriculum vita	72

List of tables

Table 3.1: The Concentration of Cu ions (M) measured by ICP at the different concentration of Ag ion in solution, 2 μ m Cu condition	23
Table 3.2: The Concentration of Cu ions (M) measured by ICP at the different concentration of Ag ion in solution, 100nm Cu condition	30
Table 3.3: The cementation ratio of Cu-Ag coreshell at the different concentrations of Ag ions	42
Table 3.4: The conductivity of Cu-Ag coreshell paste at different coreshell contents	44
Table 3.5: The conductivity of Cu-Ag coreshell paste at different sintering temperatures	46
Table 3.6: The measurement results of sprayed volume of Cu paste (cm ³) at different Cu content conditions	51
Table 3.7: The viscosity of Cu paste and $\mu/\Delta P$ at different Cu contents	53
Table 3.8: Printing parameters	56

List of figures

Figure 1.1: Existing 3D printers and 3D printable materials	2
Figure 2.1: Shrinking core model when the film diffusion control is limiting reaction rate ...	11
Figure 2.2: The concentration changes of the reactant by film diffusion control.....	12
Figure 2.3: The concentration changes of the reactant by product layer diffusion control	14
Figure 2.4: The concentration changes of the reactant by chemical reaction control.....	16
Figure 2.5: Schematic of 3D printer for high viscous materials and screw extruder.....	20
Figure 3.1: The concentration of Cu ion in solution at different Ag ion concentrations (2 μ m Cu particle condition)	22
Figure 3.2: Synthesizing reaction of Cu-Ag coreshell in the aqueous solution.....	25
Figure 3.3: Plot of log(rate) versus log($\{Ag^+\}$), 2 μ m Cu particle condition	26
Figure 3.4: Empirical conversion-time curve at 2 μ m Cu particle condition, (A) theoretical film diffusion control conversion-time curve	27
Figure 3.5: The concentration of Cu ion in solution at different Ag ion concentrations (100nm Cu particle condition)	29
Figure 3.6: SEM images and EDS analysis results of Cu particles, (A) 2 μ m Cu particle and (B) 100nm Cu particle	31
Figure 3.7: Schematic of synthesizing Cu-Ag coreshell process using 100nm Cu particles...	33
Figure 3.8: pH dependence of reaction rate, 100nm Cu particle condition	35
Figure 3.9: Empirical conversion-time curve at 100nm Cu particle condition, (A) theoretical chemical reaction control conversion-time curve	36
Figure 3.10: The concentration of Cu ions at the different concentration of Ag ions condition	38
Figure 3.11: SEM images and EDS results of synthesized Cu-Ag coreshell, (A) 2 μ m Cu particles condition and (B) 100nm Cu particles condition	40
Figure 3.12: The conductivity of Cu-Ag coreshell paste synthesized at different contents of coreshell particles.....	43
Figure 3.13: The conductivity of Cu-Ag coreshell paste sintered at different temperature	45
Figure 3.14: SEM images of sintered Cu-Ag coreshell paste at different temperature (A)400 $^{\circ}$ C, (B)450 $^{\circ}$ C, (C)500 $^{\circ}$ C and (D)550 $^{\circ}$ C	48

Figure 3.15: The time dependence of the sprayed volume of Cu paste at the different Cu content conditions	50
Figure 3.16: Plotted $\mu/\Delta P$ versus different Cu contents.....	52
Figure 3.17: The volumetric flow rate of Cu paste at different Cu contents	54
Figure 3.18: Problems during printing high viscous material without optimization of printing parameters, (A) Printing head speed and ΔP (B) fill density.....	57
Figure 3.19: 3D structures printed by using Cu paste (106 μm , 65wt.%) and screw extruder 3D printer	58
Figure 3.20: SEM images of surface of 3D metal structure, (A) before sintering process and (B) after sintering process, mag. X 3,000	60
Figure 3.21: Shrinkage factor in the paste and comparison of the final structure size at different Cu content	62
Figure 3.22: The whole fabrication process of 3D metal structures with high viscous Cu paste	63

Chapter 1

Introduction

3D printing technology has been considered the 3rd industrial revolution. Various types of 3D printing methods have been introduced and new equipment has been commercially provided. Traditional 3D printing methods can only print specific materials such as thermoplastics, UV curable ink, and metal powder [1-4]. Printing metallic 3D structure is one aspect of additive manufacturing that has gotten a lot of attention. Current processes such as SLS (selective laser sintering) and EBM (electron beam melting) methods have been using to fabricate 3D metal structures [1]. The existing 3D printers and 3D printable materials are shown in Figure 1.1.

These processes directly melt metal particles and produce 3D structure by stacking and sintering metal layers. However, these processes have some problems that make them difficult to apply to industries. The cost of the printing equipment and well as the maintenance is rather high due to the advanced laser and electron beam system. The equipment is expensive and this equipment only can print metal. It is not effective to use in machines where critical mechanical properties are required. In addition, too much time is consumed for the completion of a printed 3D structure.

For this research, to solve the current problems, high viscous, low cost, materials are applied to accessible 3D printing processes. Traditional metal 3D printers only use metal powders as printing materials, but in this research, high viscous materials including particles are used as printable materials.

Existing 3D printers



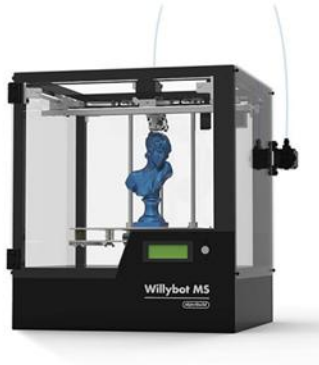
Stereolithography apparatus



Electron beam melting



UV inkjet type



Fused deposition modeling



Selective laser sintering

Existing 3D printable materials



Filament



Metal powder



UV curable ink

Figure 1.1: Existing 3D printers and 3D printable materials.

In this research work to fabricate the 3D structure by using high viscous materials and functional materials, two kind of research were performed. First, 3D printable functional material was synthesized and printed. Second, metal paste was synthesized and metal 3D printed structure was synthesized by using high viscous metal paste. The introduction about each research will be described below.

1.1 Part 1: Synthesis of functional material: Cu-Ag coreshell

In this study, coreshell was synthesized as a functional material to apply to high viscous printable material for 3D printed electronics. Coreshell has special properties including optical [5], drug storable and releasable properties [6], catalytic properties as used in organic reactions [7], specific reactivity [8] and antimicrobial property [9]. The unique characteristics of coreshell are expected to benefit multiple industries and other research fields.

Now, many methods exist for the synthesis of coreshell. For example spray pyrolysis [10], polymer shell method [11], radical polymerization [12], sono-synthesis [13] and reduction reaction method [14], have been studied. Also, to produce coreshell with stable film, many additives precursors and stabilizers are used in the synthesizing process.

In order to widen the application of coreshell to multiple industries, synthesizing processes should be simple. Synthesizing methods mentioned as above are complicated in that they involve many steps and the associated cost is high. Furthermore, if stabilizers and other additives are used to synthesize coreshell, additional processing steps are required to remove these materials making the total synthesis process more complicated. Therefore, in this study, Cu-Ag coreshell was simply prepared by using solid-liquid method without stabilizers or additives. Because of the high conductivities of these two metals, Cu-Ag coreshell is applicable to printed electronics and 3D printing technology as materials for solar cell or high viscous conductive paste. Many studies for exploiting the useful properties of Cu-

Ag coreshell have been conducted [15]. In this research, in order to compare the particle size effect on synthesis of Cu-Ag coreshell, different particle sizes of Cu particles were used. Experiments were also carried out at different Ag ion conditions to confirm the effect of Ag ion concentration in solution on the reaction rate during Cu- Ag coreshell synthesis. As a result, the difference in reaction rate between 100nm and 2 μ m particle conditions was compared and analyzed as basic research for synthesizing Cu-Ag coreshell in the point of view of reaction rate. Furthermore, to apply high viscous material Cu-Ag coreshell was mixed with high viscous flux and its electrical conductivity was also measured.

1.2 Part 2: High viscous material for 3D printing technology

The limitation of usage of 3D printable materials is the biggest problem in the 3D printing technology. In order to apply 3D printing technology to other industries and research fields, this limitation of 3D printing technology should be solved. To solve this problem, use of high viscous materials for 3D printing process is suggested and applied to this research. Because of viscosity of high viscous materials, printed structure can maintain their structure when high viscous material is printed. In addition, high viscous materials consist of powder and high viscous flux. Therefore, for example if the ceramic or metal powder is used as the powder material in the high viscous material, 3D printing process can print all of materials. Even though high viscous material does not include powder material, if high viscous material has special function itself, it can be used as 3D printable materials for special purpose.

In this study, high viscous materials were prepared and printed to confirm the efficiency of high viscous materials and optimize their printing conditions. High viscous Cu paste was prepared and printed as one of the examples of 3D printable material because of its significant applicability. Printing a metallic 3D structure is one aspect of additive manufacturing that has received a significant amount of attention. Current processes such as SLS (selective laser sintering) and EBM (electron beam melting) methods have been used to

fabricate 3D metal structures [1, 3]. These processes directly melt metal particles and produce 3D structures by stacking and sintering metal layers. However, these processes have some problems that make them difficult to apply to industries. The cost of the printing equipment and the maintenance is rather high due to the advanced laser and electron beam system. Another disadvantage is that the printing equipment can only print metal. The cost and limited printability is not effective in machines where critical mechanical properties are required. In addition, too much time is consumed for the completion of a printed 3D structure. In order to solve these current problems, high viscous, low cost materials are applied to accessible 3D printing processes. Traditional metal 3D printers only use metal powders as printing materials, but in this research, high viscous materials that mix particles and flux are used as printable materials. Usually, high viscous materials are synthesized by mixing particles, high viscous flux, and additives [16-23]. Typically, high viscous flux is prepared by using an organic solution and additives so it is hard to handle and needs special caution. However, the high viscous flux was easily synthesized by using a water soluble polymer and additives in this research. As a main printable material, Cu particles were used to synthesize a high viscous metal paste because Cu is one of the cheapest metals and has many applications due to its high electrical conductivity. [24, 25]

Traditional 3D printing methods, SLS (selective laser sintering) [26], FDM (fused deposition modeling) [27] and SLA (stereolithography apparatus) [28], can only print specially prepared materials, not high viscous materials. Therefore, other printing methods are needed in order to overcome the limits of the current technology. In order to extrude high viscous materials, another printing process involving a screw extruder was used in this research.

Following the printing of the high viscous material, after treatment should be performed because printed 3D structures using high viscous material do not harden.

Therefore, hardening processes such as UV curing, chemical or heat treatment should be used to make printed structures complete. In this study, the metal particle, Cu, was used as the main printable material, so the sintering process was conducted to harden the printed metal structure. In addition, printing parameters for the screw extruder were also optimized to print synthesized high viscous materials.

The viscosity of the material is the most significant factor since it controls the printing process and its printing parameters. Therefore, as a fundamental part of the research, the viscosity of high viscous material was measured and compared by changing the content of Cu particles in the paste.

Chapter 2

Materials and experimental procedure

2.1 Part 1: Materials

Copper oxide was reduced to Cu metal particles and then used as Cu nano particles. 2 μ m Cu particle (Nano Technology) was also used in this experiment. Hydrazine monohydrate (purity \geq 99%, Alfa Aesar) was used to reduce copper oxide and average particle size of Cu nano particle reduced by hydrazine monohydrate was 100nm. Silver nitrate (Purity \geq 99.8%, Sigma Aldrich) was used as source of Ag ions in solution.

2.2 Part 1: Experimental procedure

2.2.1 Synthesis process of Cu-Ag coreshell, analysis and theory

The concentration of Cu was fixed but particle size of Cu and concentration of Ag were experimental variables. All experiments were performed at room temperature. The synthesis process was as follows: First, a $1 \times 10^{-1} \text{ mol} \cdot \text{dm}^{-3}$, 50ml Cu particle solution was prepared by mixing 100nm Cu particles and distilled water. Next Ag ion solutions were prepared where the concentration of Ag differed for each experiment and had values of $1 \times 10^{-2} \text{ mol} \cdot \text{dm}^{-3}$, $5 \times 10^{-2} \text{ mol} \cdot \text{dm}^{-3}$, $1 \times 10^{-1} \text{ mol} \cdot \text{dm}^{-3}$, $1.5 \times 10^{-1} \text{ mol} \cdot \text{dm}^{-3}$, $2 \times 10^{-1} \text{ mol} \cdot \text{dm}^{-3}$ and $4 \times 10^{-1} \text{ mol} \cdot \text{dm}^{-3}$. When Cu solution and Ag ion solutions were mixed in each experiment, their concentration changed because total volume of solution changed from 50 ml to 100 ml. Therefore, the concentration of Cu became $5 \times 10^{-2} \text{ mol} \cdot \text{dm}^{-3}$ in the mixed solution and that of Ag ion in solution became $5 \times 10^{-3} \text{ mol} \cdot \text{dm}^{-3}$, $2.5 \times 10^{-2} \text{ mol} \cdot \text{dm}^{-3}$, $5 \times 10^{-2} \text{ mol} \cdot \text{dm}^{-3}$, $7.5 \times 10^{-2} \text{ mol} \cdot \text{dm}^{-3}$, $1 \times 10^{-1} \text{ mol} \cdot \text{dm}^{-3}$ and $2 \times 10^{-1} \text{ mol} \cdot \text{dm}^{-3}$ at 100ml solution

for each experiment. After combining the two solutions, the mixture was stirred at 300 rpm and reacted for 10 minutes. The mixture was then subjected to a centrifuge in order to separate the Cu-Ag coreshell particles from the solution at 6,000 rpm for 10 minutes. Next, the Cu-Ag coreshell was washed with distilled water after the centrifuge process was complete. The rinse water and coreshell mixture was then subjected to a centrifuge process again at the same condition. Finally the coreshell was then dried in a vacuum oven at 80°C. Experiments involving 2µm Cu particles were performed by the same process as mentioned above. Each sample was analyzed by ICP (Optima 7000 DV, Perkin Elmer) and scanning electron microscopy (TM-1000 Tabletop Microscope, Hitachi and S-4800 scanning electron microscopy, Hitachi).

Prepared Cu-Ag coreshell was mixed with high viscous flux to make Cu-Ag coreshell paste. To confirm contents effect on conductivity of paste, the content of coreshell particles in the paste was changed from 19 vol.% to 31 vol.% of Cu-Ag coreshell particles. The paste was heat treated by using a furnace (Box furnace, Lindberg/Blue M) at 500°C for 20min. In addition to confirm the effect of heat treatment temperature, the heat treatment temperature was also changed from 400°C to 550°C. The electrical conductivity of heat treated samples was measured by using 4-pin probe (LORESTA-GP MCP-T610, Mitsubishi Chemical Corporation).

2.2.2 Shrinking core model

In this research, the shrinking core model was used to determine reaction limiting steps. When the particles and reactant are reacted with each other, sometimes particles can maintain their size or decrease or increase. In this case, the rate of this reaction can be influenced by three different factors. The concentration of the reactant, the chemical reaction between two reactants, and the layer produced on the surface of particle can control the total reaction rate. This shrinking core model is developed to confirm and explain the rate control factors of the reaction which contains reaction between particles and liquid or gas. Through this theory, the reaction control factor, actually a limiting step, can be defined, and by using this confirmed step, rate of reaction can be controlled. Because of this, the shrinking core model is used in this experiment.

In order to apply the shrinking core model to the experiment, two assumptions are needed. First, the reaction should not be reversible. If the reaction is reversible the particle size cannot be formed and decreased uniformly so it is hard to calculate and estimate their expected particle size mathematically. Second, the particle shape should be spherical and the radius, R , is constant during the reaction, and the reaction interface at r_c shrinks uniformly.

There are three resistances, actually reaction rate limiting step. First, film diffusion control, second, product layer diffusion control, and third, chemical reaction control. These three kinds of limiting steps are introduced simply above. These limiting steps will be introduced in the next part.

2.2.3 Limiting step

In the shrinking core model, there are three reaction limiting steps, film diffusion control, product layer diffusion control and chemical reaction control. The rate of reaction able to apply the shrinking core model is controlled by those three limiting steps. Generally, the reaction rate is defined by the slowest reaction in the reaction. In the reaction, the three

limiting steps are able to occur, but only one limiting step, the slowest among all steps, can be the limiting step of the reaction. All limiting steps will be introduced below.

2.2.3.1 Film diffusion control

When the reactant reacts with the particles, the film diffusion layer surrounding surface of particles will be created. The film diffusion layer is shown in Figure 2.1.

In this case, the concentration of the particle depends on the radius of the particle. The concentration of the reactant, the solution or gas, is constant at the outside of film diffusion layer. However, the concentration of the reactant is controlled by film diffusion layer, and closer to the surface of the particle, lower the concentration of reactant is shown. The concentration change of the reactant is shown in Figure 2.2.

The reaction rate is controlled by the diffusion rate of the reactant in the film diffusion layer. The reaction completed time is calculated. The equation and each component are shown below.

$$t_{comp} = \frac{\rho_B R}{3bk_m C_A}$$

t_{comp} : The completed time

ρ_B : The molar density of the particle

R : The radius of the particle

b : The stoichiometry number of the reactant in the reaction

C_A : The concentration of the reactant

k_m : The mass transfer coefficient between the fluid and the particle

In addition, the radius of unreacted core in terms of fractional time for complete conversion is obtained and shown below.

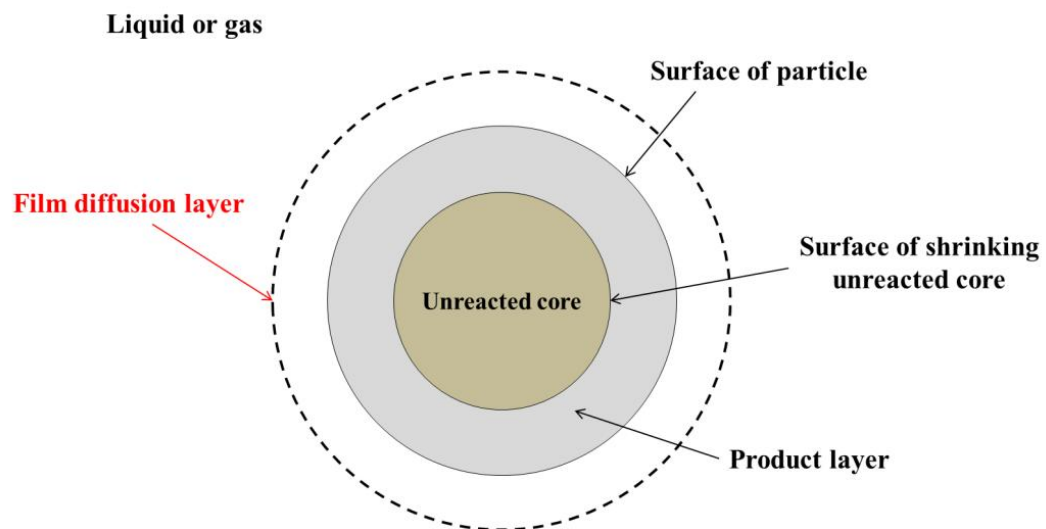


Figure 2.1: Shrinking core model when the film diffusion control is limiting the reaction rate.

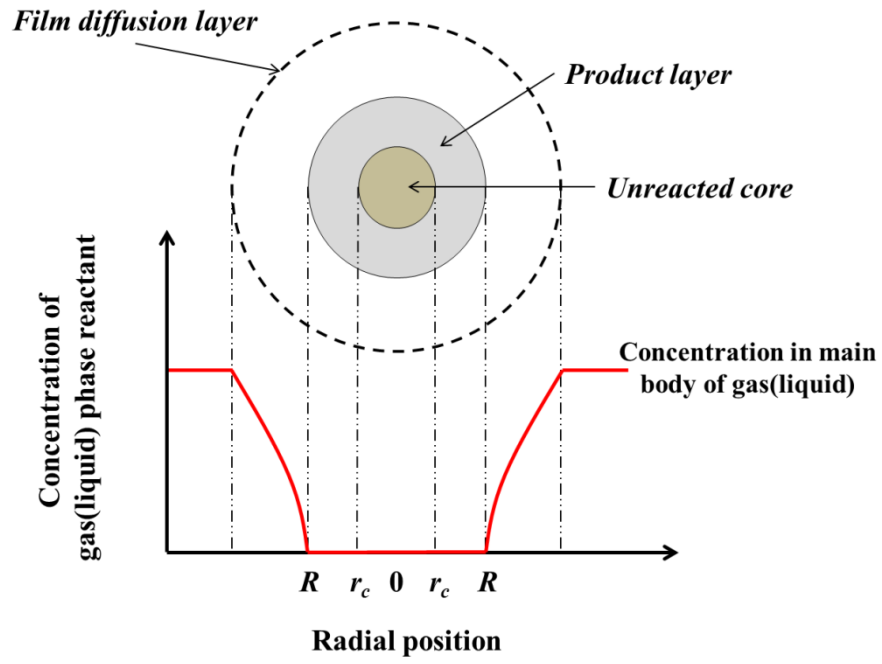


Figure 2.2: The concentration changes of the reactant by film diffusion control.

$$\frac{t}{t_{comp}} = X_B = 1 - \left(\frac{r_c}{R}\right)^3$$

t: The reaction time

t_{comp}: The Completed reaction time

X_B: The fractional conversion

r_c: The radius of unreacted particle

R: The radius of the particle

Through this equation, the relationship of time with radius and with conversion can be obtained.

2.2.3.2 Product layer diffusion control

When the diffusion through product layer is limiting the rate of the reaction, the concentration change of the reactant is changed by the effective diffusivity of the reactant. In this case the film diffusion layer is also formed around the surface of the particle, but this film diffusion layer cannot influence the concentration change of the reactant. The change of the concentration of the reactant is changed by diffusivity of the product layer. The concentration change of the reactant controlled by product layer is shown in Figure 2.3.

In this case, the completed time of the reaction can be expressed by a mathematical method, which is the expression shown below.

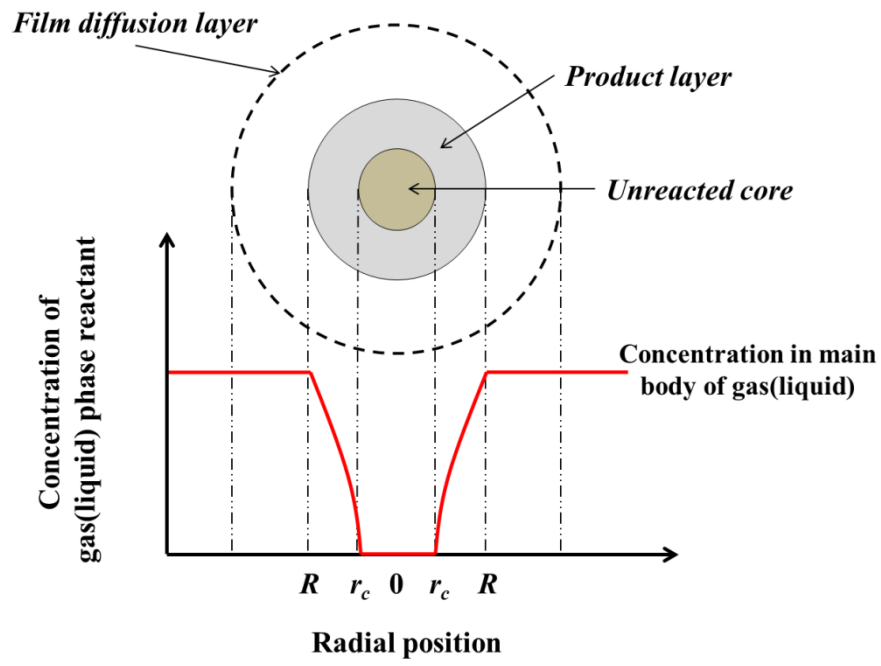


Figure 2.3: The concentration changes of the reactant by product layer diffusion control.

$$t_{comp} = \frac{\rho_B R^2}{6bD_e C_A}$$

t_{comp} : The completed time

ρ_B : The molar density of the particle

R : The radius of the particle

b : The stoichiometry number of the reactant in the reaction

C_A : The concentration of the reactant

D_e : The effective diffusion coefficient

In addition, the completed time is also expressed in terms of fractional conversion.

The equation is shown below.

$$\frac{t}{t_{comp}} = 1 - 3(1 - X_B)^{\frac{2}{3}} + 2(1 - X_B) = 1 - 3\left(\frac{r_c}{R}\right)^2 + 2\left(\frac{r_c}{R}\right)^3$$

Each component is the same as noticed in the film diffusion control part.

2.2.3.3 Chemical reaction control

When the rate of the reaction is controlled by chemical reaction control, the reaction rate is not affected by film diffusion layer and product layer. Therefore, the reaction rate is proportional to the available surface of unreacted particle. Figure 2.4 shows the concentration change of the reactant in the chemical reaction control. In this case the reaction rate is related to the first-order rate constant for the surface reaction. The expressed completed time of this limiting control is shown below.

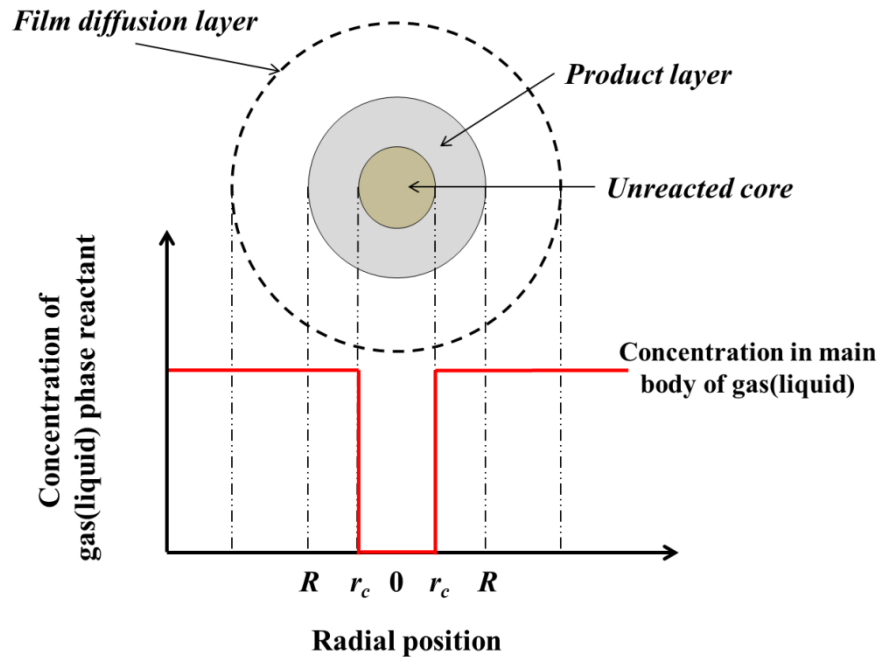


Figure 2.4: The concentration changes of the reactant by chemical reaction control.

$$t_{comp} = \frac{\rho_B R}{b k'' C_A}$$

t_{comp} : The completed time

ρ_B : The molar density of the particle

R: The radius of the particle

b: The stoichiometry number of the reactant in the reaction

C_A : The concentration of the reactant

k'' : The first order rate constant

The fractional conversion term of the equation is shown below too.

$$\frac{t}{t_{comp}} = 1 - (1 - X_B)^{\frac{1}{3}} = 1 - \frac{r_c}{R}$$

Each component is same as noticed in the film diffusion control part.

2.3 Part 2: Materials

Copper particles were used to synthesize a high viscous metal paste. 106 μ m (Acros Organics, 99%, powder) and 25 μ m (Sigma Aldrich, 99%, powder) of copper particles were applied. Polyvinyl carboxy polymer (MakingCosmetics) and PVA (polyvinyl alcohol, Fisher Science Education) was used as a viscosity enhancement reagent in the high viscous flux.

2.4 Part 2: Experimental procedure

2.4.1 Synthesis of high viscous Cu paste

To prepare the high viscous material, the viscosity enhancement reagent, 7 wt.% of polyvinyl carboxy polymer, was dissolved in water. In addition, the pH of the solution was controlled to 7 by using sodium hydroxide and then stirring until the solution transformed into gel. After preparing the gel, PVA was dissolved in the water and then 7 wt.% of the PVA solution was prepared. After making two kinds of materials, the polyvinyl carboxy polymer gel and the PVA solution were mixed to make a high viscous flux at the specific ratio (polyvinyl carboxy polymer:PVA = 95:5). After the two polymers were completely mixed, the Cu powder was added to the prepared high viscous flux. The contents of Cu changed to 50, 55, 60 and 65 wt.%. Cu particles and the high viscous material were thoroughly mixed and then the Cu paste was kept from any further air contact.

2.4.2 Viscosity measurement

The prepared high viscous metal paste was printed by using an extruder type 3D printing machine. By using this equipment, the viscosity of metal paste could be obtained by using Hagen-Poiseuille equation [29]. The equation is shown below:

$$Q = \frac{\pi r^4 \Delta P}{8 \mu L}$$

Q: The volumetric flow rate

L: The length of tip

R: The radius of tip

ΔP : The difference of pressure between the end and top of the tip

μ : The viscosity of material.

In this experiment the volumetric flow rate was measured every minute. It was performed for a total of 5 minutes and the measured volumetric flow was plotted. The slope was determined by the volumetric flow rate. The radius (1 mm) and the length (13 mm) of the tip were fixed respectively. ΔP was calculated by using the viscosity-known material (viscosity range: 3,700,000~3,800,000 cP). However, ΔP can be changed by materials, $\mu/\Delta P$ was expressed as an expression of viscosity of high viscous materials in the experiment.

2.4.3 3D printing process and heat treatment

In order to print the high viscous metal paste and construct metal 3D structures, an extruder type of printing machine was developed and a FDM 3D printer (Opencreators, NP-mendel) was modified and connected to the extruder. The schematic of 3D printing equipment is shown in Figure 2.5. Printing conditions were optimized according to the viscosity. All of printed metal 3D structures were air dried at room temperature and heat treated with charcoal by using a box furnace (Box furnace, Lindberg/Blue M) at 950 °C for two hours.

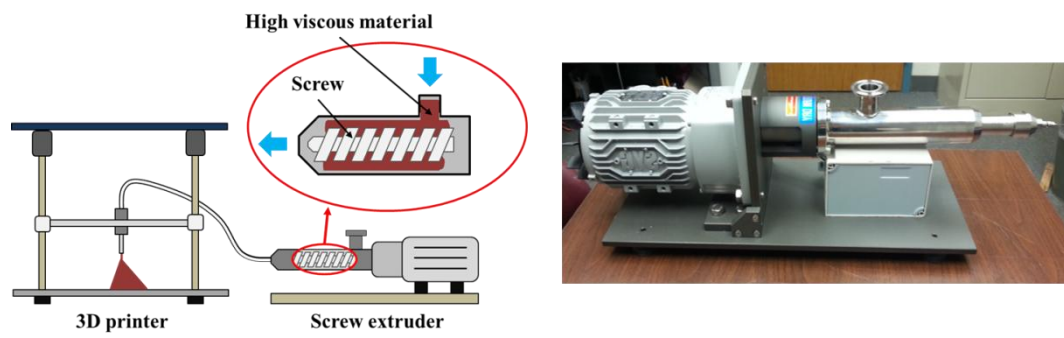


Figure 2.5: Schematic of 3D printer for high viscous materials and screw extruder.

Chapter 3

Results and discussion

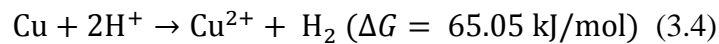
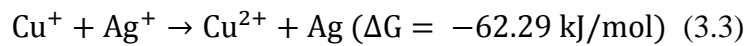
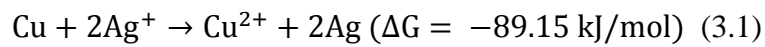
Part 1: Synthesis of functional material: Cu-Ag coreshell

3.1 The limiting step of reaction

In this study, Cu-Ag coreshell was synthesized by using 2 μ m and 100nm Cu particles without any additives and stabilizers. The concentration of produced Cu ions was measured by ICP analysis and the change in concentration of Cu ions at 2 μ m Cu conditions is shown in Figure 3.1, and the measured concentration of Cu ion is also shown at Table 3.1.

Based on Figure 3.1, it can be confirmed that the reaction was finished between 5 and 10 seconds for the 2 μ m Cu particle condition for all concentrations of Ag ion. In Figure 3.1, it is observable that the concentration of produced Cu ions and reaction rate increases as the concentration of Ag ions increases.

The reaction rate was calculated and the order of reaction was also calculated by based on the changes of concentration of Cu ions. In this experiment, 4 reactions can occur in solution and the reaction equations for this experiment are as follows:



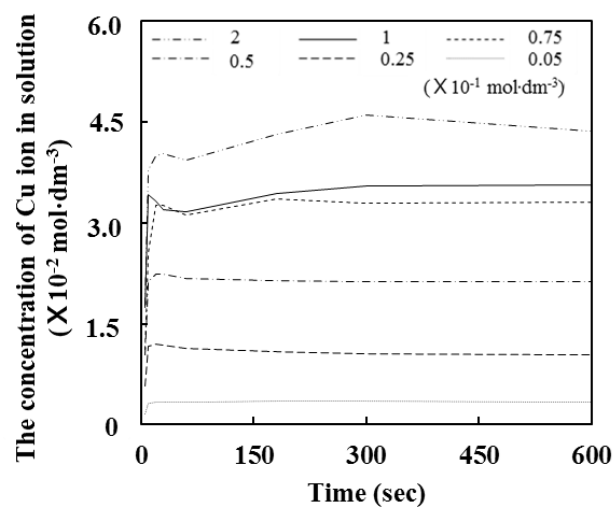


Figure 3.1: The concentration of Cu ion in solution at different Ag ion concentrations ($2\mu\text{m}$ Cu particle condition).

Table 3.1: The Concentration of Cu ions (M) measured by ICP at the different concentration of Ag ion in solution, 2 μ m Cu condition.

Concentration of Cu ion (M)		0.005	0.025	0.05	0.75	0.1	0.2
Time (sec)	5	0.003277	0.011419	0.021477	0.022453	0.034195	0.035469
	10	0.003583	0.011958	0.022266	0.0285	0.034211	0.040313
	20	0.003611	0.011966	0.02293	0.036719	0.032164	0.039703
	30	0.003777	0.011628	0.022305	0.028297	0.031703	0.040719
	60	0.003302	0.011002	0.021328	0.034016	0.031539	0.037844
	180	0.003084	0.010778	0.021227	0.033031	0.03707	0.048344
	300	0.002982	0.01042	0.019398	0.032859	0.033984	0.043547
	600	0.003408	0.010313	0.021328	0.033266	0.037313	0.043547

When calculating Gibbs free energy, the reaction described by equation (3.1) is the predominant reaction as compared to the other reactions, and this reaction in the solution is shown in Figure 3.2.

Therefore, equations (3.2) and (3.3) are not considered. In addition, because of the Gibbs free energy, equation (3.4) cannot occur meaning that hydrogen ion cannot influence this reaction. The Concentration of Cu ($5 \times 10^{-2} \text{ mol} \cdot \text{dm}^{-3}$, 100 ml) was fixed in reaction equation above, therefore the concentration of Cu can be considered as a rate constant in this rate equation. The rate equation can be expressed as is seen below.

$$\frac{d\{Cu^{2+}\}}{dt} = k'\{Ag^+\}^l \quad (3.5)$$

The order of reaction for each condition was calculated and is plotted in Figure 3.3. The order of reaction was determined to be 0.65 for the $2\mu\text{m}$ Cu particle. In order to confirm which step was the limiter of the reaction rate at this condition, the shrinking core model was applied in this paper. Analysis of the conversion-time curve was used to confirm limiting step of this reaction. Through analysis of this curve, the reaction rate limiting step can be determined [30]. In Figure 3.4, the conversion-time curve is expressed and compared with theoretical curve.

When the conversion-time curve plot (generated by experimental data) is compared with the theoretical curve in Figure 3.4, the tendency of $2\mu\text{m}$ Cu particle curve is the same as film diffusion control curve. Seemingly, the reaction rate of $2\mu\text{m}$ Cu particles is limited by film diffusion control.

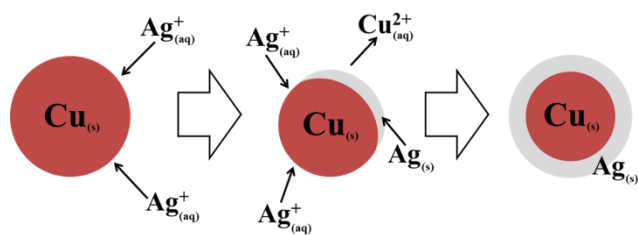


Figure 3.2: Synthesizing reaction of Cu-Ag coreshell in the aqueous solution.

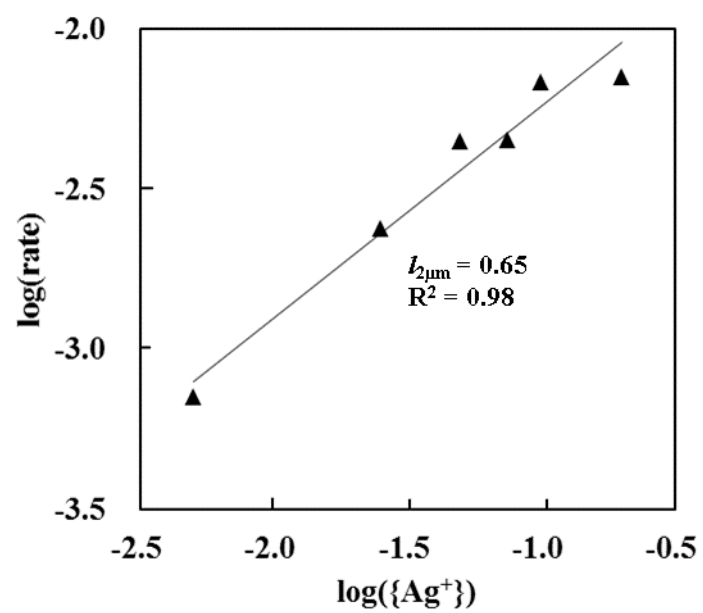


Figure 3.3: Plot of $\log(\text{rate})$ versus $\log(\{\text{Ag}^+\})$, $2\mu\text{m}$ Cu particle condition.

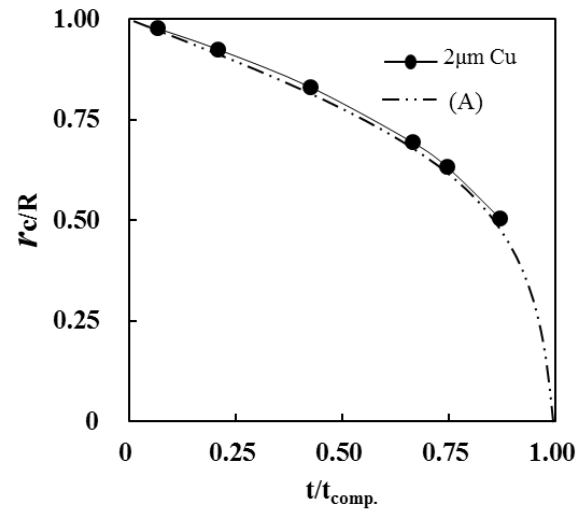


Figure 3.4: Empirical conversion-time curve at 2μm Cu particle condition, (A) theoretical film diffusion control conversion-time curve.

In Figure 3.5, the change in concentration of produced Cu ions for experiments involving 100nm Cu particles is shown, and the measured data is shown in the Table 3.2. According to Figure 3.5, the reaction went along continuously when 100nm Cu particles were used. In addition, as shown in Figure 3.1, the reaction was quickly finished when 2 μ m Cu particles were used, but in the case of experiments involving 100nm Cu particles, the reaction was not quickly finished. Generally, when particles are of a small size, the reaction rate will increase because surface area will increase too. However, a 100nm particle is 20 times smaller than a 2 μ m Cu particle in this case. Nevertheless, the reaction rate of the 100nm Cu condition was slower than that of the 2 μ m Cu condition. This result occurs due to the presence of CuO film on surface of 100nm Cu particles.

Nano-sized Cu particle can be easily oxidized in an ambient environment. According to previous research, to prevent Cu nano particles from oxidizing, the pressure of oxygen should be controlled at 2.6×10^{-45} atm in air [31]. Controlling the oxygen pressure mentioned before is impossible, and it means that oxidation of Cu nano particles cannot be prevented in air. From this result, it seems that when 100nm Cu particles are prepared to synthesize Cu-Ag coreshell the surface of Cu nano particle is oxidized, and at the same time CuO film is formed on the surface before 100nm Cu particles react with Ag ion solution.

Through SEM and EDS analysis, it was confirmed that 100nm Cu particles were already oxidized about 2 wt.% but 2 μ m Cu particles were not. The EDS and SEM results of 2 μ m and 100nm Cu particles are shown at Figure 3.6.

Through Pilling-Bedworth ratio, R_{PB} , the stability of copper oxide film was checked [32]. R_{PB} of copper oxide is 1.6. Thus, copper oxide film is a stable and passivating film capable of providing a protective effect. For this reason, Ag ions cannot diffuse to copper through copper oxide film formed on surface of 100nm Cu particles.

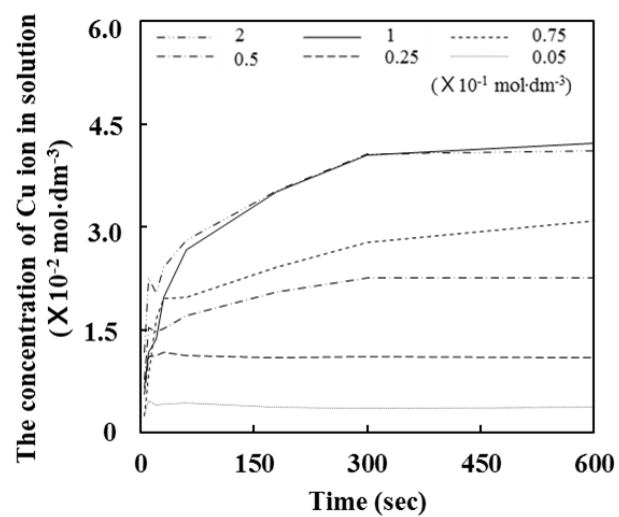


Figure 3.5: The concentration of Cu ion in solution at different Ag ion concentrations (100nm Cu particle condition).

Table 3.2: The Concentration of Cu ions (M) measured by ICP at the different concentration of Ag ion in solution, 100nm Cu condition.

Concentration of Cu ion (M)		0.005	0.025	0.05	0.75	0.1	0.2
Time (sec)	5	0.005016	0.010268	0.015816	0.007732	0.017584	0.023594
	10	0.004545	0.010358	0.014763	0.017464	0.015005	0.021625
	20	0.004213	0.010401	0.014744	0.025492	0.017016	0.019281
	30	0.004835	0.009216	0.015805	0.021195	0.024266	0.028938
	60	0.003322	0.008249	0.018352	0.023969	0.032016	0.027234
	180	0.002698	0.010499	0.022734	0.028352	0.039057	0.043313
	300	0.002854	0.010991	0.022313	0.029977	0.041578	0.038016
	600	0.003091	0.010892	0.022906	0.032211	0.042411	0.044203

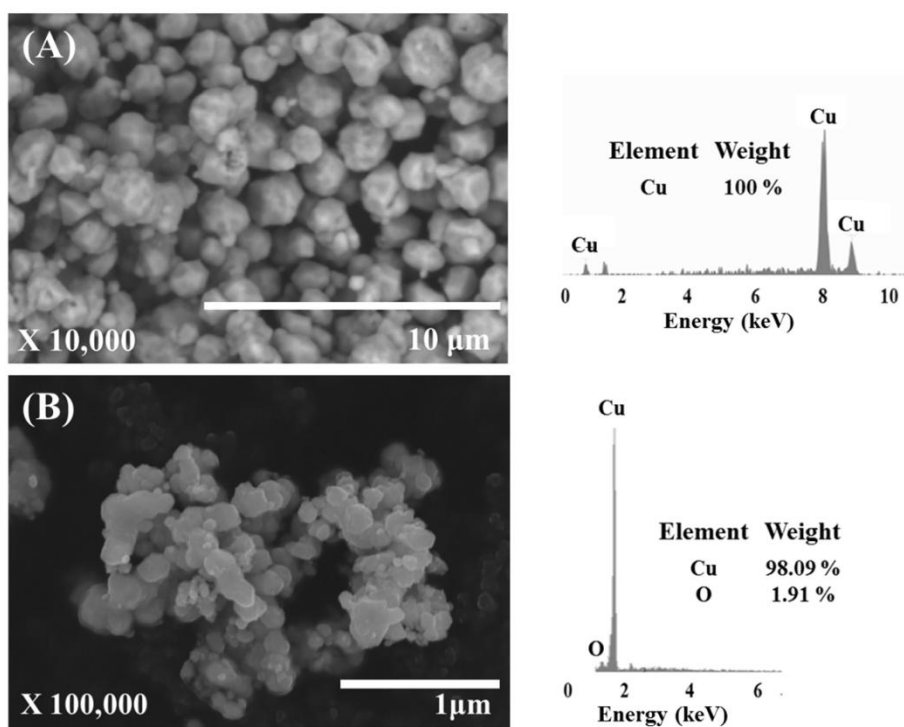
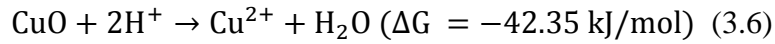


Figure 3.6: SEM images and EDS analysis results of Cu particles, (A) 2 μm Cu particle and (B) 100nm Cu particle.

In this condition, the pH of solution is between 4.67 and 5.89 at a concentration of Ag ions between $2 \times 10^{-1} \text{ mol} \cdot \text{dm}^{-3}$ and $5 \times 10^{-3} \text{ mol} \cdot \text{dm}^{-3}$. The surface charge of copper oxide is positive in this pH range [33], so Ag ions are not adsorbed on surface of copper oxide film. Therefore, in this condition, the reaction described by equation (3.1) can occur and another reaction can occur in solution described by the following equation:



In this case, it can be considered that equation (3.4) cannot occur, because of its Gibbs free energy. Because of the low pH condition, copper oxide film reacts with acid in solution and then copper oxide becomes copper ion and these Cu ions are released in solution (equation (3.6)). At this time, a pure Cu surface will be exposed, Ag ions and the newly exposed Cu surface can then react in solution and allowing for Ag film to be coated on the surface of Cu (equation (3.1)). This reaction occurs continuously and finally Cu-Ag coreshell is synthesized in solution. In Figure 3.7, the schematic of this reaction is shown.

Roughly 2 wt.% of Cu was oxidized, but it was not partially oxidized. Because all 100nm Cu particles were oxidized as much as 2 wt.% and formed copper oxide film, the reaction using 100nm Cu particles was slower than the reaction using 2 μm Cu particles which were not oxidized. In order to synthesize Cu-Ag coreshell by using 100nm Cu particles, the copper oxide film must be removed first.

In this reaction, the pH of solution can influence on the reaction (equation (3.5)). Therefore, the total reaction rate is limited by the reaction between copper oxide film and hydrogen ion in solution. In order to increase the reaction rate in this condition, copper oxide film should be removed fast, and pH control can be used to dissolve copper oxide film. The reaction rate of equation (3.5) was measured at different pH conditions.

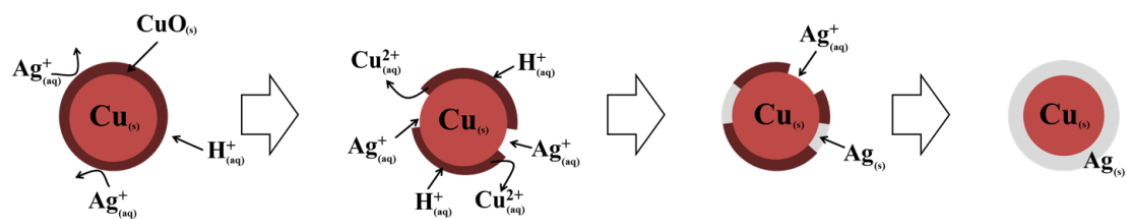


Figure 3.7: Schematic of synthesizing Cu-Ag coreshell process using 100nm Cu particles.

The results of pH dependence of reaction rate are shown in Figure 3.8. In Figure 3.8, it can be confirmed that as the pH of solution decreases, the reaction rate of equation (3.6) increases. In addition, it was considered that the concentration of Ag ions in solution cannot influence this reaction rate because when 2 μ m was applied, reaction was quickly finished. As a result, the rate equation can be expressed as is seen below.

$$\frac{d\{\text{Cu}^{2+}\}}{dt} = k'\{\text{H}^+\}^l \quad (3.7)$$

The order of reaction was also calculated to be ~ 0.2 ($R^2 = 97\%$) for the 100nm Cu particle condition. This reaction is that of copper oxide on the surface of 100nm Cu particles reacting with hydrogen ions in solution. Product layer control cannot limit this reaction rate because the reaction occurs on the surface. Thus, it can be expected that equation (3.6) can be governed by film diffusion control or chemical reaction control. In order to confirm which limiting step is truly controlling this reaction rate, analysis of the conversion-time curve was again used, and then experimental curve was compared to theoretical curve. In Figure 3.9, these two curves are expressed. As shown in Figure 3.9, the tendency of conversion-time curve behavior for equation (3.6) is the same as the conversion-time curve for chemical reaction control. Therefore, when 100nm Cu particles are used to synthesize Cu-Ag core-shell, the entire reaction rate is controlled by equation (3.6). In addition, the reaction rate of equation (3.6) is limited by chemical reaction control.

When the concentration of Ag ions was $1 \times 10^{-1} \text{ mol} \cdot \text{dm}^{-3}$ and $2 \times 10^{-1} \text{ mol} \cdot \text{dm}^{-3}$ as seen in Figure 3.5, the concentration of produced Cu ions in solution was the same for these concentrations. For the 2 μ m Cu particle condition seen in Figure 3.1, as the concentration of Ag ions increases, the concentration of produced Cu ions also increases. However, for the 100nm Cu particle condition seen in Figure 3.5, when the concentration of Ag ions is under $1 \times 10^{-1} \text{ mol} \cdot \text{dm}^{-3}$, the concentration of produced Cu ions increases as the concentration of Ag ions increases.

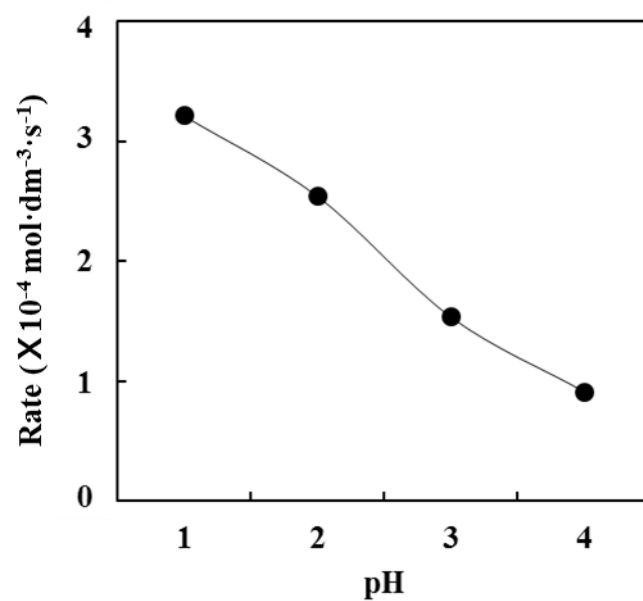


Figure 3.8: pH dependence of reaction rate, 100nm Cu particle condition.

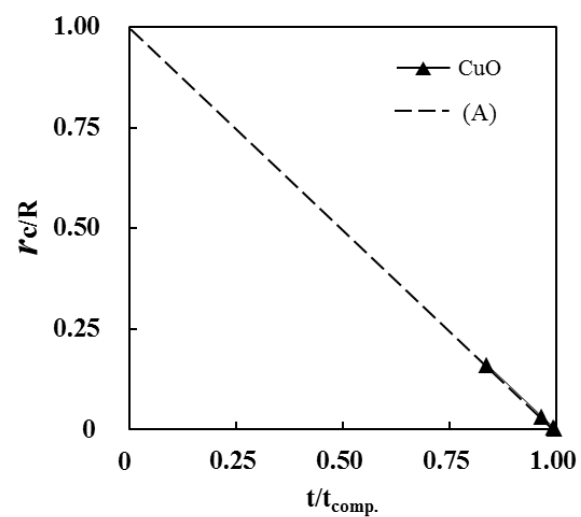


Figure 3.9: Empirical conversion-time curve at 100nm Cu particle condition, (A) theoretical chemical reaction control conversion-time curve.

This means that a stable Cu-Ag coreshell which does not react with Ag ions in solution is synthesized when 100nm Cu particle is used with $1 \times 10^{-1} \text{ mol} \cdot \text{dm}^{-3}$ concentration of Ag ion. If Cu-Ag coreshell synthesized in $1 \times 10^{-1} \text{ mol} \cdot \text{dm}^{-3}$ Ag ion concentration is stable, the concentration of produced Cu ions at a higher concentration of Ag ion conditions should be maintained as same as $1 \times 10^{-1} \text{ mol} \cdot \text{dm}^{-3}$ condition. In order to confirm, Cu-Ag coreshell was synthesized at higher concentration of Ag ions. In Figure 3.10, results are shown.

In the case of 100nm Cu particles, the concentration of Cu ions did not increase at $1 \times 10^{-1} \sim 6 \times 10^{-1} \text{ mol} \cdot \text{dm}^{-3}$, and the concentrations of Cu ions measured at different concentrations of Ag ions were similar. However, the concentration of Cu ion increased between 1×10^{-1} and $2 \times 10^{-1} \text{ mol} \cdot \text{dm}^{-3}$ conditions in $2\mu\text{m}$ Cu particle, and the other results were similar to those observed for the 100nm Cu particle conditions. Therefore, stable Cu-Ag coreshell can be synthesized in 100nm Cu particles with $1 \times 10^{-1} \text{ mol} \cdot \text{dm}^{-3}$ of Ag ions or $2\mu\text{m}$ with $2 \times 10^{-1} \text{ mol} \cdot \text{dm}^{-3}$ of Ag ions. According to this result, it was confirmed that when concentration of Ag ions is $1 \times 10^{-1} \text{ mol} \cdot \text{dm}^{-3}$, the Cu-Ag coreshell synthesized at $2\mu\text{m}$ Cu particle condition is less stable as compared to the 100nm Cu particle condition because the concentration of Cu ions in solution increases as the concentration of Ag ions increases.

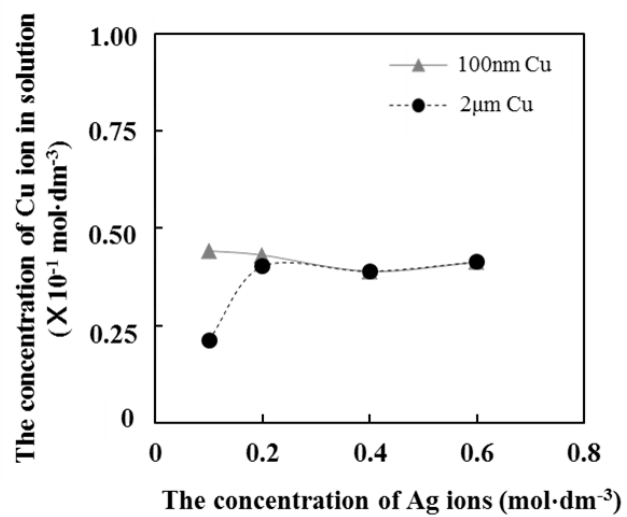


Figure 3.10: The concentration of Cu ions at the different concentration of Ag ions condition.

3.2 The shape and cementation ratio of Cu-Ag coreshell

A SEM micrograph of prepared Cu-Ag coreshell was also taken in order to confirm the morphology of Cu-Ag coreshell used 2 μ m and 100nm Cu particles and is seen in Figure 3.11.

When SEM micrographs for the two particle size conditions are compared in Figure 3.11, it is notable that the morphology of synthesized coreshell was spherical for the 2 μ m Cu particle size condition, but when 100nm Cu particles were applied, the synthesized Cu-Ag coreshell had dendrite structure. Disk shape of Cu-Ag coreshell was also observed in the two conditions.

The difference of shape in formation of Cu-Ag coreshell is resulted by different reaction rates affected by existence of CuO film on the surface. Actually, the reaction rate of 2 μ m Cu particle is much faster than that of 100nm particle condition. In the 2 μ m Cu particle condition, Ag metal rapidly covers to the surface of Cu particles because 2 μ m Cu particles have no CuO film on their surface so that Ag ions in the solution can react fast without any obstacle. Because of rapid reaction rate, the Cu-Ag coreshell has no time and chance to grow and form to the specific shape. Therefore, the Cu-Ag coreshell can form spherical shape the most stable shape in this 2 μ m Cu particle condition. The reaction rate of 100nm Cu particle condition is relatively slower than that of 2 μ m Cu particle condition because of existence of CuO film on the surface of Cu nano particle. Therefore, when the Ag ions react to Cu nano particles, the approaching to Cu surface of Ag ion is disturbed by CuO film. The part of the CuO film is slowly dissolved and removed by reacting with acid in the solution, and then the surface of pure Cu will be exposed. At that time Ag ions can react with the pure Cu surface.

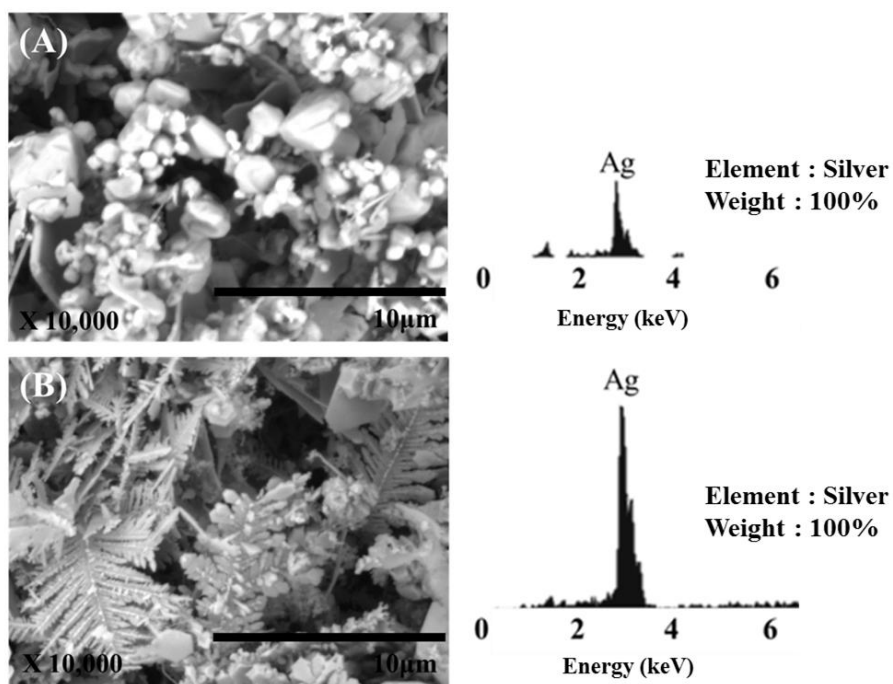


Figure 3.11: SEM images and EDS results of synthesized Cu-Ag coreshell, (A) 2μm Cu particles condition and (B) 100nm Cu particles condition.

During Ag is reduced on the part of Cu surface, the other part of CuO film also will be removed and then Ag ions will react with other exposed pure Cu surface. While this process is repeated, the Ag formed on the first exposed part of Cu surface can grow continuously and the other parts which were covered by Ag metal later also can. Therefore, the Cu-Ag coreshell using 100nm Cu particle can have enough time to grow to produce a dendrite shape. It is possible because this reaction is controlled by CuO film on the surface of Cu nano particles. From this result, it was confirmed that even though same method was used to synthesize Cu-Ag coreshell, their particle shape can be changed by reaction rate controlled by CuO film and particle size.

The cementation ratio of the Cu-Ag coreshell was also calculated. The result is shown in the Table 3.3. In 2 μ m and 100nm Cu particle size condition, when the concentration of Ag ion in solution increased, the cementation ratio of Ag on the Cu-Ag coreshell also increased.

3.3 Electrical conductivity measurement

The conductivity of Cu-Ag coreshell was measured by using a 4-pin probe. Cu-Ag coreshell paste was synthesized and its particle content was changed. In Figure 3.12, the result of conductivity measurement was shown and Table 3.4 shows the measurement result of conductivity of coreshell paste at different coreshell contents. The conductivity of the coreshell paste increased as content of coreshell particles in the paste increased. In addition the conductivity at 31 vol.% was 10 times higher than the conductivity at 19 vol.%. This paste had 4% of conductivity of bulk silver metal ($6.3 \times 10^5 \text{ S} \cdot \text{cm}^{-1}$) [34]. In this experiment, the maximum content which can mix with high viscous flux was 31 vol.%. In order to increase conductivity of paste sintering temperature was changed, but the particle content was fixed to the highest content, 31 vol.%. The conductivity results of paste sintered at different temperature are shown in Figure 3.13 and Table 3.5.

Table 3.3: The cementation ratio of Cu-Ag coreshell at the different concentrations of Ag ions.

Conditions	2 μ m Cu		100nm Cu	
Concentration of Ag ion (M)	Cu (wt.%)	Ag (wt.%)	Cu (wt.%)	Ag (wt.%)
0.005	84.68	15.32	79.68	20.32
0.025	52.98	47.02	51.86	48.14
0.05	28.51	71.49	25.97	74.03
0.075	12.99	87.01	13.48	86.52
0.1	9.16	90.84	4.73	95.27
0.2	1.01	98.99	3.74	96.26

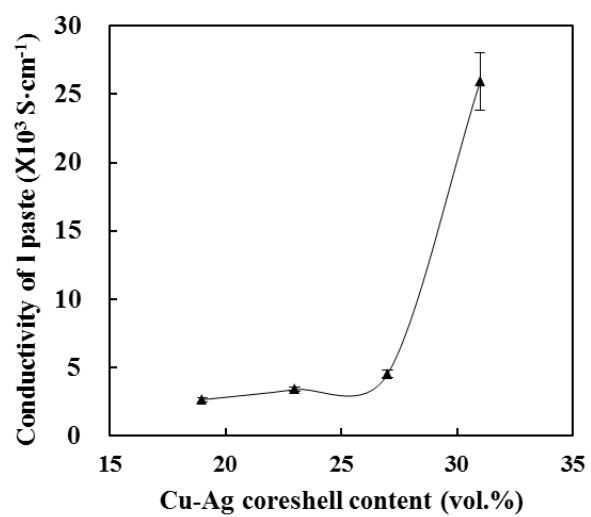


Figure 3.12: The conductivity of Cu-Ag coreshell paste synthesized at different contents of coreshell particles.

Table 3.4: The conductivity of Cu-Ag coreshell paste at different coreshell contents.

Content of Cu-Ag coreshell (vol.%)	Conductivity (S/cm)
19	2649
23	3388.2
37	4508
31	25926

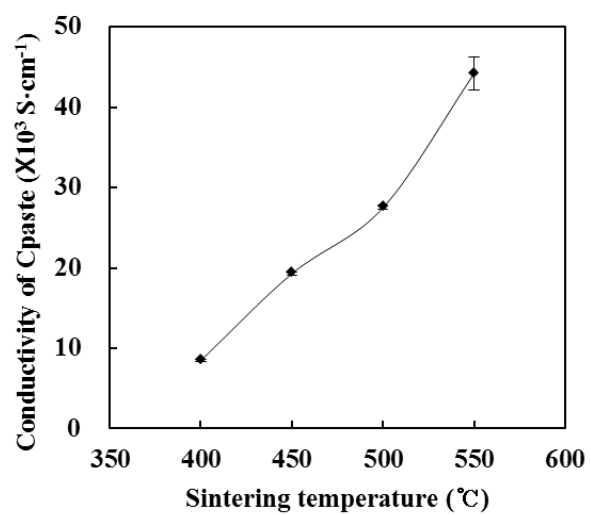


Figure 3.13: The conductivity of Cu-Ag coreshell paste sintered at different temperature.

Table 3.5: The conductivity of Cu-Ag coreshell paste at different sintering temperatures.

Content of Cu-Ag coreshell (vol.%)	Conductivity (S/cm)
19	8473.6
23	19287
37	27506
31	44196

The conductivity of coreshell paste increased as sintering temperature increased. It means that the coreshell particles are more connected each other at the high sintering temperature, so that it can have higher conductivity than the other conditions even they have same particle content in the paste. The conductivity was 7% of that of bulk Ag metal at highest sintering temperature condition. The surfaces of sintered coreshell paste are shown in Figure 3.14.

According to Figure 3.14, at the low temperature, 400°C and 450°C, most particles are melted. They are not perfectly connected each other and just have some small neck between coreshell particles. However, at the other conditions, 500°C and 550°C, the particles are connected well, and most of particles are melted and connected, finally they formed thin layer. That kind of thin layer could be observed in all of temperature conditions, and it was much more formed and observed as increasing sintering temperature. Cu-Ag coreshell thin layer is formed a lot, and they can connect each other easily at the high sintering temperature condition. For this reason the conductivity of paste increased as sintering temperature increased even though all of the surface of sintered paste were porous and had some cracks.

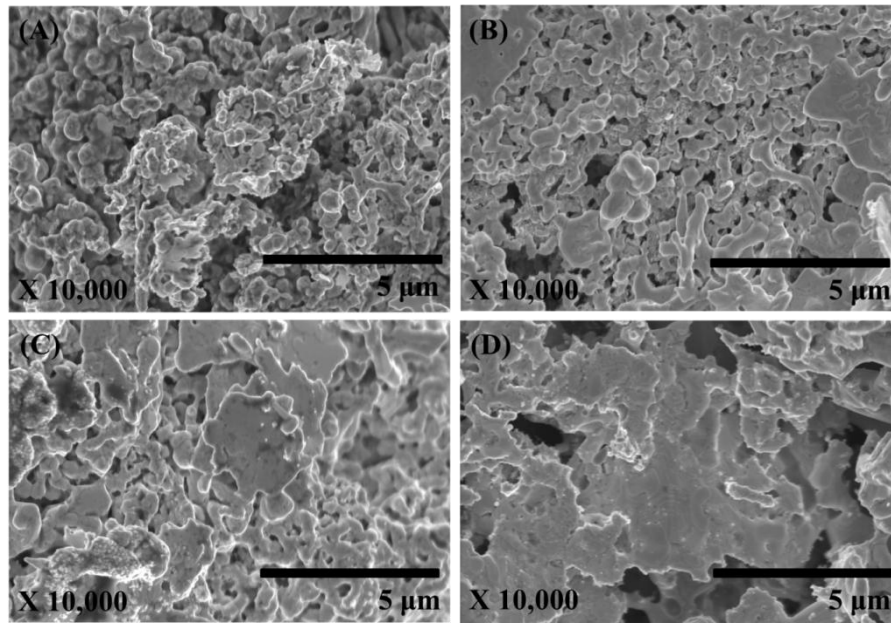


Figure 3.14: SEM images of sintered Cu-Ag coreshell paste at different temperature

(A)400°C, (B)450°C, (C)500°C and (D)550°C.

Part 2: High viscous material for 3D printing technology

3.4 Viscosity of high viscous Cu paste

Before the viscosity was measured, it was confirmed whether Cu paste was Newtonian fluid or not. If this Cu paste is not Newtonian fluid, Hagen-Poiseuille equation cannot be used to measure viscosity of synthesized Cu paste. Therefore, in order to confirm this one, the volume of the sprayed Cu paste at the different Cu content condition was measured. The volume verses time graph was plotted to confirm whether the graph is linear function and the graph is linear function, this Cu paste functioned as Newtonian fluid. This result is shown in Figure 3.15 and Table 3.6. In all of conditions, the plotted graph has linear function, the prepared Cu paste is considered as Newtonian fluid in this research. The viscosity of the paste was measured by using the Hagen-Poiseuille equation. The result of the measurement ($\mu/\Delta P$) is shown in Figure 3.16 and the specific data is shown in Table 3.7.

The measured $\mu/\Delta P$ values increased as the content of Cu in the paste increased. It means that the viscosity of the Cu paste increased as the Cu contents increased. By using viscosity-known materials the absolute viscosity of the Cu paste was calculated. The highest viscosity was around 2.3×10^7 cP. The packing ratio between the flux and the particles changed because of the addition of Cu particles. In this case, as the metal content increased, the fluidity of the paste decreased. The fluidity of paste can directly influence the printing speed. Figure 3.17 shows the measurement of the volumetric flow rate of the Cu paste. The volumetric flow rate dropped dramatically (from 50 to 55 wt.% Cu), while the other conditions gradually dropped. The entire volumetric flow rate of the Cu paste decreased as the metal content increased. This means that when viscosity of paste is high, the material can have a low volumetric flow rate, which causes a decrease in the printing speed. In order to increase the printing speed, the viscosity of the paste should decrease.

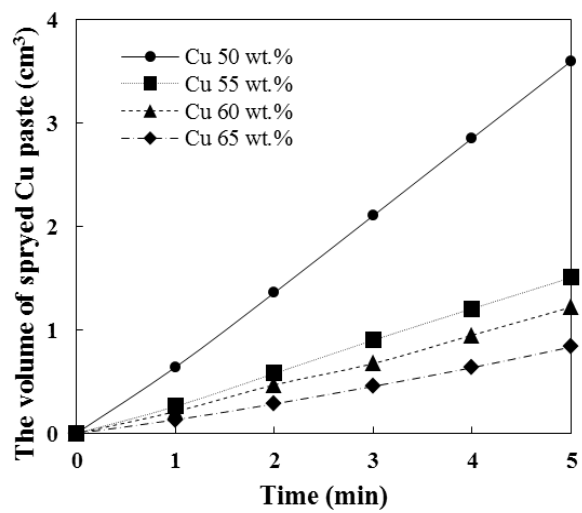


Figure 3.15: The time dependence of the sprayed volume of Cu paste at the different Cu content conditions.

Table 3.6: The measurement results of sprayed volume of Cu paste (cm³) at different Cu content conditions.

Cu content (wt.%)		50	55	60	65
Time (min)	1	0.639	0.260	0.211	0.131
	2	1.359	0.580	0.469	0.285
	3	2.105	0.901	0.675	0.455
	4	2.854	1.207	0.950	0.636
	5	3.599	1.506	1.220	0.836

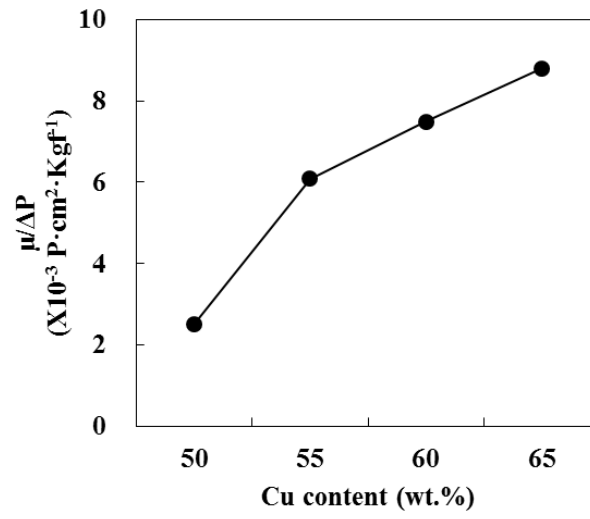


Figure 3.16: Plotted $\mu/\Delta P$ versus different Cu contents.

Table 3.7: The viscosity of Cu paste and $\mu/\Delta P$ at different Cu contents.

Cu content (wt.%)	50	55	60	65
$\mu/\Delta P$ ($P \cdot cm^2 \cdot Kgf^{-1}$)	0.0025	0.0061	0.0075	0.0088
Calculated viscosity (cP)	6,975,583	16,808,201	20,768,557	23,242,575

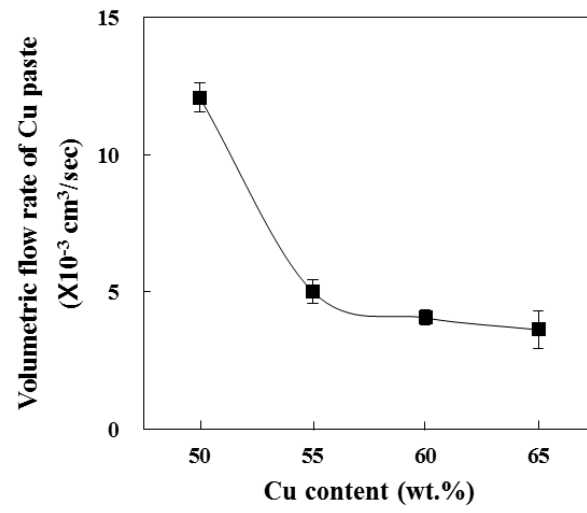


Figure 3.17: The volumetric flow rate of Cu paste at different Cu content.

3.5 Printing process and optimization of parameters for 3D metal structure

3D metal structures were printed by the using the high viscous Cu paste and the screw extruder 3D printer. In order to obtain a fine 3D metal structure, printing conditions were changed as shown in Table 3.8.

In order to adjust the printing head speed and screw rpm (control quantity of printed paste), the rpm of screw extruder was fixed but only the printing head speed was changed. Because fill density can affect the quality of final structure, this parameter was also changed in this experiment. These parameters are very important for printing high viscous materials because unlike traditional 3D printing processes, such as FDM, the printed material does not solidify quickly. Therefore, if the printing speed is too fast, the printed layers could disconnect. In addition, if the fill density is too low, the printed layers cannot be stacked properly (or the printed layers would collapse) and the final structure cannot be printed the same as the 3D modeling generated in the CAD (computer aided software).

If the fill density is too high, each of the printed layers can overlap, compromising the integrity. When patterns are overlapped, the excess printed material will remain in the printed layer and will push outward from each other. These excess materials can cause an expansion of each printed layer. Thus, if the fill density and the printing speed are not optimized, fine products cannot be fabricated using the high viscous materials. Examples of these problems are shown below in Figure 3.18.

In order to print the prepared Cu paste, printing conditions were optimized. Printing head speeds were controlled every 6-8 mm/sec, and fill density was controlled between 75 - 85%, which was a suitable condition to print fine 3D structures. Printed 3D structures using high viscous Cu paste are shown in Figure 3.19.

Table 3.8: Printing parameters.

Printing Parameter	Condition
Tip size	500 μm
Printing head speed	2 ~ 10 mm/s
Layer height	0.4 mm
Fill density	50 ~ 90 %
rpm (ΔP , screw extruder)	45 rpm

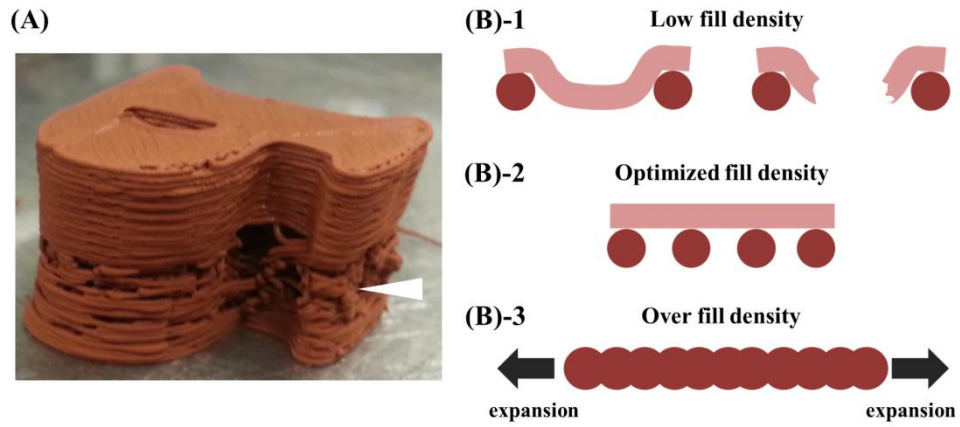


Figure 3.18: Problems during printing high viscous material without optimization of printing parameters, (A) Printing head speed and ΔP (B) fill density.



Figure 3.19: 3D structures printed by using Cu paste (106 μm , 65wt.%) and screw extruder 3D printer.

After printing the 3D structures, they were heat treated. Because of the heat treatment, the surface of the sintered 3D metal structure was not clean and the size of final product shrank. In order to measure the shrinkage of the final product, cylinder shaped structures were printed and heat treated. After this process, the volume of the printed cylinder was measured. The volume of the final structure was reduced to 25% of its original volume. During the heat treatment process, evaporation of the high viscous flux and binder will occur, which creates a lot of void spaces between the layers and metal particles. In addition, the distance between metal particles decreased because metal particles were melted and formed necks. Metal particles can connect, but because of the empty spaces resulting from high flux ratio in the paste, the size of final structure was reduced. In Figure 3.20, SEM images of the surface of the 3D structure can be seen.

In Figure 3.20 (A), there is a large amount of empty space, but the structure can maintain its shape because of high viscous flux and binder in the paste. In Figure 3.20 (B), the surface of the 3D structure has less empty space than (A) and the particles of (B) are well connected to each other. Therefore, during the sintering process, metal particles fill the empty space. For this reason, the size of the final product decreased. After heat treatment, some samples had cracks on the surface of product. This is a result of the rapid shrinkage that occurred during the heat treatment process, which also caused a relatively high content of flux. Therefore, in order to reduce the defects and shrinkage of the final product, less flux should be used and the metal content should increase.

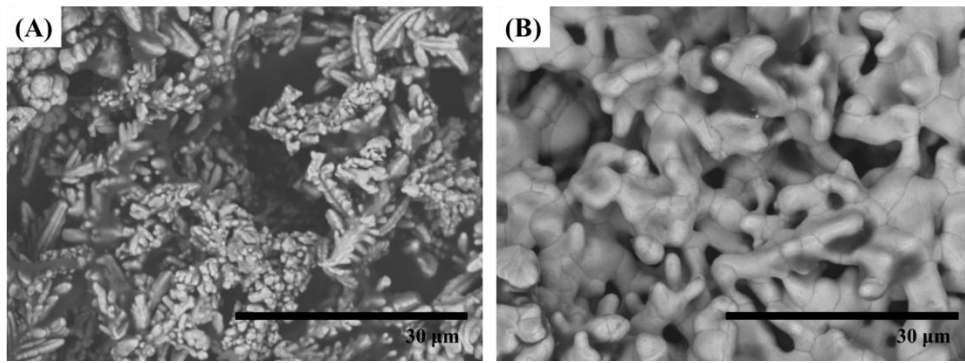


Figure 3.20: SEM images of surface of 3D metal structure, (A) before sintering process and (B) after sintering process, mag. X 3,000.

3.6 Packing factor effect on fabrication of 3D metal structures

To prevent the formation of defects and impact from shrinking, high metal content Cu paste was prepared. 25 μ m size Cu particles were mixed with a high viscous flux. A maximum 86 wt.% Cu particles could be mixed in the flux. However, 86 wt.% of Cu paste was too thick and its adhesion was too weak, so 82 wt.% Cu paste was printed using a screw extruder. In this part of the experiment, the packing factor of the Cu paste was changed by using different particle sizes. In order to confirm the effect of the packing factor versus the shrinkage of the final product, 106 μ m and 25 μ m of Cu were mixed at different ratios (106 μ m : 25 μ m = 7:3 and 3:7). A total of 4 kinds of Cu paste were synthesized and printed. In addition, the same printing conditions were applied and adjusted to print the Cu paste. The sintering process was also conducted using the same conditions. After the heat treatment process, the volume of the final structure was measured. The volume of the final product was roughly between 25-77% of its original 3D modeling size. By decreasing the Cu particle size and increasing the small particle ratio in the paste, the Cu content can increase from 65 wt. % to 82 wt.% which, in turn, reduces the shrinkage of the final product. The measured shrinkage factor at different Cu contents is shown in Figure 3.21. Figure 3.21 shows how the shrinkage factor decreased as the Cu content increased in the paste. Increasing Cu content causes an increase of the packing factor in the Cu paste. The Cu paste, which has a high packing factor, should be used to reduce the shrinkage of the final product. By applying the information from this result, the shrinkage of final structure can be prevented or reduced. The whole process for fabricating metal 3D structures required both the extruder printing process and the sintering process, in order to obtain a fine product free of small cracks or defects. As one of the treatment methods, a simple polishing process was performed. After finishing, the rough surface of the product was properly cleaned. The whole fabrication process of the 3D metal structure is shown in Figure 3.22.

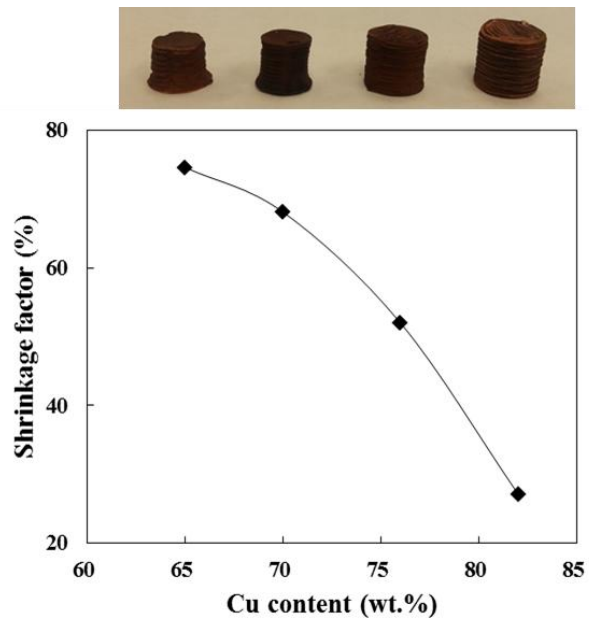


Figure 3.21: Shrinkage factor in the paste and comparison of the final structure size at different Cu content.



Figure 3.22: The whole fabrication process of 3D metal structures with high viscous Cu paste.

Chapter 4

Conclusion

In this study, two kinds of research were performed. In aspect of synthesizing 3D printable functional materials, Cu-Ag coreshell particle was synthesized and this coreshell particle was mixed with high viscous flux to prepare conductive paste. In addition, to solve the limitation of usage of 3D printable materials, High viscous Cu metal paste was also synthesized as an example of 3D printable high viscous materials and printed by using screw extruder printer.

First, in the Cu-Ag coreshell part, two different sizes of Cu particle were used to prepare Cu-Ag coreshell. In terms of the reaction rate, as increasing concentration of Ag ions in the solution, both reaction rates also increased. However, the reaction rate of 2 μ m Cu condition was faster than that of 100nm Cu condition. Because of CuO film on the 100nm Cu particles, slow reaction rate in the 100nm Cu condition was measured. Through shrinking core model theory reaction rate limiting step was confirmed. When 2 μ m Cu particle was used to prepare the Cu-Ag coreshell, it is confirmed that the reaction rate was controlled by film diffusion control. In the 100nm Cu condition, the reaction react was controlled by CuO film on the surface of the Cu nano particle. This CuO film was dissolved by acid in the solution, the rate of this reaction is limited by chemical reaction control.

The shape of the synthesized Cu-Ag coreshell has spherical in the 2 μ m Cu condition, and dendrite-shaped Cu-Ag coreshell was formed in the 100nm Cu condition. In addition, the more stable Cu-Ag coreshell, which does not react with Ag ions in the solution in the high Ag ion concentration, could be synthesized when 100nm Cu was applied. The Cu-Ag coreshell paste was prepared at the different coreshell contents. The conductivity of Cu-Ag coreshell paste increased as volume of Cu-Ag coreshell particles in the paste increased.

The conductivity of the highest particle content was 10 times higher than that of the lowest condition. In this case, however, the conductivity was only 4% of conductivity of bulk silver. As the sintering temperature increased, the conductivity also increased. The conductivity of the highest sintering temperature condition was 4.6 times higher than that of the lowest condition. In this case, the conductivity of the coreshell paste has 7% of the conductivity bulk Ag metal. In order to apply this material to 3D printable materials, high viscous flux suitable for this particle should be developed and then increasing content of particle in the paste should be necessary. In addition, this synthesis method can be used to control shape of coreshell particle in terms of synthesis of functional material.

Second, high viscous Cu paste was synthesized and printed using a screw extruder type of 3D printer. As a fundamental aspect of this research, the viscosity of the Cu paste was measured using the Hagen-Poiseuille equation and equipment because the viscosity of the 3D printable high viscous materials is hard to measure using existing methods. As the Cu content increased, the viscosity of the Cu paste also increased and the viscosity of the printed paste was 2.3×10^7 cP at 65 wt.% of Cu. The materials, which had an extremely high viscosity, can be measured through this viscosity measurement method. In addition, printing parameters can also be optimized through changing the viscosity of materials. To print high viscous Cu paste, the printing conditions were also optimized to attain an adequate 3D structure. In this case, the suitable printing speed was 6-8 mm/sec and the fill density was 75-85%.

The sintering process was used as one of the after treatment methods. After sintering, the shrinkage of the final product was observed. The shrinkage factor decreased as the Cu particle contents increased. In this study, 23% of the shrinkage factor was obtained at the highest Cu content condition. In addition, it was confirmed that as the particle size decreased, the maximum content of the Cu in the paste increased. Also, when 106 μm and 25 μm of Cu particles were mixed to modify the packing factor of Cu paste and increase Cu content, the

Cu content of the paste increased as the ratio of smaller particles in the paste increased. Therefore, in order to prevent the shrinkage of the final product, the packing factor of Cu paste should increase and the ratio of flux in the metal paste should decrease.

After sintering, in order to remove the cracks after treatment, polishing was conducted because it is one of the surface treatment methods of the metal. According to the printed materials, this final step can be changed. Therefore, after treatment methods (suitable for the specific materials) should be developed, in order to improve quality of the final 3D structure using high viscous materials.

The printing processes and parameters can be changed by viscosity, and the quality of the 3D structure can also be changed by viscosity. The viscosity can be affected by various factors including the packing factor, the particle size, the shape, and the component of high viscous flux. The viscosity of materials and the factors affecting the viscosity are significant elements in the 3D printing technology that uses high viscous materials. Therefore, in order for further research work to improve and apply these materials and processes effectively, the relationship between viscosity and the factors affecting viscosity of materials should be analyzed and studied thoroughly. In addition, the prototype of the 3D printer for high viscous materials, the screw extruder, was used in this research to display the printed products. In order to improve the quality and accuracy of the final products, printing equipment with optimal printing conditions should be developed.

References

- [1] Hernandez, S.J. Li, E. Martinez, L. E. Murr, X.M. Pan, K.N. Amato, X.Y. Cheng, F. Yang, C.A. Terrazas, S.M. Gaytan, Y.L. Hao, R. Yang, F. Medina, and R.B. Wicker, “Microstructures and Hardness Properties for β -Phase Ti–24Nb–4Zr–7.9Sn Alloy Fabricated by Electron Beam Melting,” *Journal of Materials Science & Technology* 29 (2013): 1011-1017.
- [2] N. Mostafa, H. M. Syed, S. Igor, and G. Andrew, “A Study of Melt Flow Analysis of an ABS-Iron Composite,” *Tsinghua Science and Technology* 14 (2009): 29-37.
- [3] F. Xie, X. He, S. Cao and X. Qu, “Structural and mechanical characteristics of porous 316L stainless steel fabricated by indirect selective laser sintering,” *Journal of Materials Processing Technology* 213 (2013): 838-843.
- [4] A. Bertsch, H. Lorenz, and P. Renaud, “3D microfabrication by combining microstereolithography and thick resist UV lithography,” *Sensors and Actuators A: Physical* 73 (1999): 14-23.
- [5] B. Saraswathi Amma, K. Manzoor, K. Ramakrishna, and M. Pattabi, “Synthesis and optical properties of CdS/ZnS coreshell nanoparticles,” *Materials Chemistry and Physics* 112 (2008): 789-792.
- [6] X. Chen, “Core/shell structured silica spheres with controllable thickness of mesoporous shell and its adsorption, drug storage and release properties,” *Colloids and Surfaces A: Physicochemical and Engineering Aspects* 428 (2013): 79-85.
- [7] Z. Zhang, H. Che, Y. Wang, J. Gao, Y. Ping, Z. Zhong, and F. Su, “Template-free synthesis of Cu@Cu₂O core–shell microspheres and their application as copper-based

- catalysts for dimethyldichlorosilane synthesis” *Chemical Engineering Journal* 211-212 (2012): 421-431.
- [8] N. Singh, A. Ponzoni, R.K. Gupta, P.S. Lee, and E. Comini, “Synthesis of In₂O₃–ZnO core–shell nanowires and their application in gas sensing,” *Sensors and Actuators B: Chemical* 160 (2011): 1346-1351.
- [9] A.M. Abdel-Mohsen, R.M. Abdel-Rahman, R. Hrdina, A. Imramovský, L. Burgert, and A.S. Aly, “Antibacterial cotton fabrics treated with core–shell nanoparticles,” *International Journal of Biological Macromolecules* 50 (2012): 1245-1253.
- [10] K.C. Pingali, S. Deng, and D.A. Rockstraw, “Direct synthesis of Ru–Ni core-and-shell nanoparticles by spray-pyrolysis: Effects of temperature and precursor constituent ratio,” *Powder Technology* 183 (2008): 282-289.
- [11] M. Ghahari, P. Fabbri., F. Pilati, L. Pasquali, M. Montecchi, and R. Aghababazadeh, “Highly luminescent yttria–silica core–shell nanoparticles by the sacrificial polymer shell method,” *Ceramics International* 39 (2013): 4513-4521.
- [12] H.S. Hwang, J.H. Bae, H.G. Kim, and K.T. Lim, “Synthesis of silica–polystyrene core–shell nanoparticles via surface thiol-lactam initiated radical polymerization,” *European Polymer Journal* 46 (2010): 1654-1659.
- [13] N. Ghows, and M.H. Entezari, “Sono-synthesis of core–shell nanocrystal (CdS/TiO₂) without surfactant,” *Ultrasonics Sonochemistry* 19 (2012): 1070-1078.
- [14] R. Feng, M. Li, and J. Liu, “Synthesis of core–shell Au@Pt nanoparticles supported on Vulcan XC-72 carbon and their electrocatalytic activities for methanol oxidation,” *Colloids and Surfaces A: Physicochemical and Engineering Aspects* 406 (2012): 6-12.

- [15]H.T. Hai, H. Takamura, and J. Koike, “Oxidation behavior of Cu–Ag core–shell particles for solar cell applications,” *Journal of Alloys and Compounds* 564 (2013): 71-77.
- [16]J. H. Sohn, L. Q. Pham, H. S. Kang, J. H. Park, B. C. Lee, and Y. S. Kang, “Preparation of conducting silver paste with Ag nanoparticles prepared by e-beam irradiation,” *Radiation Physics and Chemistry* 79 (2010): 1149-1153.
- [17]H.K. Park, B.S. Kong, and E.S. Oh, “Effect of high adhesive polyvinyl alcohol binder on the anodes of lithium ion batteries,” *Electrochemistry Communications* 13 (2011): 1051-1053.
- [18]D. Wakuda, K.S. Kim, and K. Suganuma, “Ag Nanoparticle Paste Synthesis for Room Temperature Bonding,” *IEEE Transactions on Components and Packaging Technologies* 33 (2010): 437-442.
- [19]K. Park, D. Seo, and J. Lee, “Conductivity of silver paste prepared from nanoparticles,” *Colloids and Surfaces A: Physicochemical and Engineering Aspects* 313-314 (2008): 351-354.
- [20]A. S. Ionkin, B. M. Fish, Z. R. Li, L. Liang, M. E. Lewittes, L. K. Cheng, C. Westphal, J. G. Pepin, and F. Gao, “Quaternary phosphonium salts as cationic selective dispersants in silver conductive pastes for photovoltaic applications,” *Solar Energy Materials and Solar Cells* 124 (2014): 39-47.
- [21]R.H. McCurdy, A.R. Hutchinson, and P.H Wiinfield, “The mechanical performance of adhesive joints containing active disbonding agents,” *International Journal of Adhesion and Adhesives* 46 (2013): 100-113.
- [22]P. Hass, O. Kläusler, S. Schlegel, P. Niemz, “Effects of mechanical and chemical surface preparation on adhesively bonded wooden joints,” *International Journal of Adhesion and*

Adhesives 51 (2014): 95-102.

- [23]K. S. Siow, “Mechanical properties of nano-silver joints as die attach materials,” *Journal of Alloys and Compounds* 514 (2012): 6-19.
- [24]Y.H. Kim, B.Y. Lee, S.N. Yang, I.B. Jeong, and S.M. Cho, “Use of copper ink for fabricating conductive electrodes and RFID antenna tags by screen printing,” *Current Applied Physics* 12 (2012): 473-478.
- [25]M.M. Haque, D. Cho, and C. S. Lee, “Investigation of sintering behavior of octanethiol-coated copper nano ink under various atmospheres,” *Thin Solid Films* 536 (2013): 32-38.
- [26]E. O. Olakanmi, “Selective laser sintering/melting (SLS/SLM) of pure Al, Al–Mg, and Al–Si powders: Effect of processing conditions and powder properties,” *Journal of Materials Processing Technology* 213 (2013): 1387-1405.
- [27]A. Kantaros, and D. Karalekas, “Fiber Bragg grating based investigation of residual strains in ABS parts fabricated by fused deposition modeling process,” *Materials & Design* 50 (2013): 44-50.
- [28]K. F. Leong, C. S. Chua, G. S. Chua, and C. H. Tan, “Abrasive jet deburring of jewellery models built by stereolithography apparatus (SLA),” *Journal of Materials Processing Technology* 83 (1998): 36-47.
- [29]H.L. Dryden, F.D. Murnaghan, H. Bateman, *Hydrodynamics*. (Dover, New York, 1956)
- [30]O. Levenspiel, *Chemical Reaction Engineering*, 3rd edn. (John Wiley & Sons, New York 1999), 566-588.
- [31]K. Han and N. Kim, “Challenges and Opportunities in Direct Writing Technology Using Nano-metal Particles,” *KONA Powder and Particle Journal* 27 (2009): 73-83.

- [32]C. Xu, and W. Gao, "Pilling-Bedworth ratio for oxidation of alloys," *Materials Research Innovations* 3 (2000): 231-235.
- [33]J.A. Lewis, "Colloidal Processing of Ceramics," *Journal of the American Ceramic Society* 83 (2000): 2341-2359.
- [34]N.S. Kim, and K.N. Han, "Future Direction of Direct Writing," *Journal of Applied Physics* 108 (2010): 102801-102801-6.

Curriculum vita

In 1987, Seongik Hong was born in Seoul, South Korea. He graduated from Chungwon High School, Seoul, South Korea. In spring 2006, he entered Seokyeong University, Seoul, South Korea. In 2008-2009, he finished his military service. While he was completing a bachelor's degree in Chemical and Biological Engineering, he worked as a research assistant in KEN Research Center (Korea Environment and Nano Research Center) for 2 years (2010-2012). During working as a research assistant, he managed 1 research project and participated in two projects, and one paper was published as a coauthor. After receiving his bachelors of engineering in 2012, he worked for Korea Printed Electronics Research Association for a year as a researcher. In 2013, he enrolled in graduate school at the University of Texas at El Paso as an international student. During his master program in Department of Metallurgical and Materials Engineering, he worked as research assistant and teaching assistant in PNE Lab (Printing Nano Engineering Lab). He published four papers as a first author and coauthor and presented in two conferences. He won "John R. Serrano Memorial Endowed Copper Research Award" and "Graduate Research Award" from Department of Metallurgical and Materials Engineering in 2014.

Permanent Address:

1424-606

Sanggye-dong, Nowon-gu, Seoul

South Korea, 139-200

Or

hong.sung.ik@gmail.com

shong2@miners.utep.edu